



# Unveiling the Structure and Reactivity of Fatty-Acid Based (Nano)materials Thanks to Efficient and Scalable $^{17}\text{O}$ and $^{18}\text{O}$ -Isotopic Labeling Schemes

Jessica Špačková, Charlyn Fabra, Sébastien Mitteleite, Emeline Gaillard, Chia-Hsin Chen, Guillaume Cazals, Aurélien Lebrun, Saad Sene, Dorothée Berthomieu, Kuizhi Chen, et al.

## ► To cite this version:

Jessica Špačková, Charlyn Fabra, Sébastien Mitteleite, Emeline Gaillard, Chia-Hsin Chen, et al.. Unveiling the Structure and Reactivity of Fatty-Acid Based (Nano)materials Thanks to Efficient and Scalable  $^{17}\text{O}$  and  $^{18}\text{O}$ -Isotopic Labeling Schemes. *Journal of the American Chemical Society*, 2020, 142 (50), pp.21068-21081. 10.1021/jacs.0c09383 . hal-03117231

**HAL Id: hal-03117231**

**<https://hal.umontpellier.fr/hal-03117231>**

Submitted on 7 May 2021

**HAL** is a multi-disciplinary open access archive for the deposit and dissemination of scientific research documents, whether they are published or not. The documents may come from teaching and research institutions in France or abroad, or from public or private research centers.

L'archive ouverte pluridisciplinaire **HAL**, est destinée au dépôt et à la diffusion de documents scientifiques de niveau recherche, publiés ou non, émanant des établissements d'enseignement et de recherche français ou étrangers, des laboratoires publics ou privés.

# Unveiling the structure and reactivity of fatty-acid based (nano)materials thanks to efficient and scalable $^{17}\text{O}$ and $^{18}\text{O}$ -isotopic labeling schemes

Jessica Špačková,<sup>a</sup> Charlyn Fabra,<sup>a</sup> Sébastien Mittlelette,<sup>a</sup> Emeline Gaillard,<sup>a</sup> Chia-Hsin Chen,<sup>a</sup> Guillaume Cazals,<sup>b</sup> Aurélien Lebrun,<sup>b</sup> Saad Sene,<sup>a</sup> Dorothée Berthomieu,<sup>a</sup> Kuizhi Chen,<sup>c</sup> Zhehong Gan,<sup>c</sup> Christel Gervais,<sup>d</sup> Thomas-Xavier Métro,<sup>b,\*</sup> Danielle Laurencin<sup>a,\*</sup>

<sup>a</sup> ICGM, Univ Montpellier, CNRS, ENSCM, Montpellier, France

<sup>b</sup> IBMM, Univ Montpellier, CNRS, ENSCM, Montpellier, France

<sup>c</sup> National High Magnetic Field Laboratory (NHMFL), Florida State University, Tallahassee, FL, USA

<sup>d</sup> Laboratoire de Chimie de la Matière Condensée de Paris (LCMCP), UMR 7574, Sorbonne Université, CNRS, 75005 Paris, France

**KEYWORDS.** *Fatty acid, isotopic labeling, oxygen-17, oxygen-18, solid state NMR, metal soap, nanoparticle, ZnO, ball-milling, mechanochemistry.*

---

## Abstract

Fatty acids are ubiquitous in biological systems and widely used in materials science, including for the formulation of drugs and the surface-functionalization of nanoparticles. However, important questions regarding the structure and reactivity of these molecules are still to be elucidated, including their mode of binding to certain metal cations or materials surfaces. In this context, we have developed novel, efficient, user-friendly and cost-effective synthetic protocols based on ball-milling, for the  $^{17}\text{O}$  and  $^{18}\text{O}$  isotopic labeling of two key fatty acids which are widely used in (nano)materials science, namely stearic and oleic acid. Labeled molecules were analyzed by  $^1\text{H}$  and  $^{13}\text{C}$  solution NMR, IR spectroscopy and mass spectrometry (ESI-TOF and LC-MS), as well as  $^{17}\text{O}$  solid state NMR (for the  $^{17}\text{O}$  labeled species). In both cases, the labeling procedures were scaled-up to produce up to gram quantities of  $^{17}\text{O}$ - or  $^{18}\text{O}$ -enriched molecules in just half-a-day, with very good synthetic yields (all  $\geq 84\%$ ) and enrichment levels (up to 46 % per carboxylic oxygen). The  $^{17}\text{O}$ -labeled oleic acid was then used for the synthesis of a metal soap (Zn-oleate) and the surface-functionalization of ZnO nanoparticles (NPs), which were characterized for the first time by high-resolution  $^{17}\text{O}$  NMR (at 14.1 and 35.2 T). This allowed very detailed insight into (i) the coordination mode of the oleate ligand in Zn-oleate to be achieved (including information on Zn...O distances), and (ii) the mode of attachment of oleic-acid at the surface of ZnO (including novel information on its photoreactivity upon UV-irradiation). Overall, this work demonstrates the high interest of these fatty acid-enrichment protocols for understanding the structure and reactivity of a variety of functional (nano)materials systems using high resolution analyses like  $^{17}\text{O}$  NMR.

---

## Introduction

Fatty acids are a key family of biomolecules. They are the object of numerous investigations in life sciences, notably in fields like lipidomics which focus on understanding the networks of the complete set of lipids produced in a given cell or organism.<sup>1</sup> They are also widely studied in nutrition science, due to the biological importance of  $\omega_3$  polyunsaturated fatty acids (PUFAs) like linolenic, eicosapentaenoic (EPA) and docosahexaenoic (DHA) acids.<sup>2</sup> Moreover, the amphiphilic nature of these molecules has been widely exploited for the preparation of soaps,<sup>3</sup> the formation of vesicles (including ufasomes) and drug-carrier systems,<sup>4-6</sup> and the surface-functionalization of inorganic materials and nanoparticles.<sup>7-12</sup>

Due to the importance of fatty acids, the synthesis of isotopically-labeled versions of these molecules has been looked into, as a means to investigate in more detail their structure and reactivity,<sup>13-16</sup> or to study their biological properties and metabolic pathways.<sup>17-21</sup> In particular,  $^{13}\text{C}$  isotopic labeling was found to be valuable for studying by  $^{13}\text{C}$  solid state NMR the mode of binding of the carboxylic group of stearic acid at the surface of zirconia as a function of temperature,<sup>13</sup> or the partitioning of myristate and hexanoate ligands at the surface of CdSe nanocrystals.<sup>12</sup> However, although such high-sensitivity NMR analyses are of general interest for gaining insight into the nature of organic-mineral interfaces between fatty acids and inorganic phases, their use has been scarce. This can be explained by

several factors, including the cost and limited availability of some of the commercial fatty acids enriched in  $^{13}\text{C}$ , and the time and experimental constraints for performing the labeling (whether using chemical or biological synthetic routes).<sup>21-25</sup> In this context, being able to have access more straightforwardly to isotopically-enriched fatty acids to perform high resolution spectroscopic analyses of the local binding mode of carboxylic functions at materials interfaces appears as a major objective.

When considering the different enrichment possibilities for NMR studies of fatty acids, oxygen-17 is a highly attractive target. Indeed, high-resolution  $^{17}\text{O}$  NMR spectroscopy is increasingly being used for structural elucidation purposes,<sup>26-31</sup> due to the very broad range of variation of  $^{17}\text{O}$  chemical shift (which exceeds 2000 ppm) and quadrupolar parameters (oxygen-17 has a nuclear spin of 5/2).<sup>26-27, 32</sup> However, the major drawback of this isotope is its very poor natural abundance (only 0.04%), meaning that the synthesis of  $^{17}\text{O}$ -labeled species is generally necessary. This is often seen as an obstacle due to the high costs of  $^{17}\text{O}$ -enriched precursors (1 g of  $^{17}\text{O}$ -enriched water, labeled at 90% in oxygen-17, costs 1600-2000 €), combined to the lack of straightforward and affordable labeling procedures to prepare them. In the specific case of fatty acids, the main drawbacks of current labeling protocols include the small amount of enriched molecule produced, the duration of the protocols, and/or the limited availability of the precursors used and constraints related to their manipulation, even in some of the most recent studies.<sup>33-35</sup>

Mechanochemistry is a synthetic approach which is finding an increasing number of applications in molecular and (nano)materials science.<sup>36-37</sup> In techniques like ball-milling, the mechanical energy of the milling beads is transferred to solid reagents by impact and shear forces,<sup>38</sup> in order to: (i) reduce the size of the particles, (ii) mix them efficiently, and (iii) create reactive interfaces allowing the formation of products. The addition of very small amounts of liquid is common, as it often allows accelerating the reactions, and can also help control the outcome of the products.<sup>37, 39-41</sup> In such reaction conditions, which are known as “Liquid Assisted Grinding” (LAG), less than 1  $\mu\text{L}$  of liquid per mg of powder is needed. Recently, we demonstrated that it is possible to use  $^{17}\text{O}$ -enriched water in LAG, to play the role of both a grinding assistant and reagent, and enrich in oxygen-17 a selection of organic and inorganic compounds of synthetic interest.<sup>42-43</sup> The protocols developed were found to surpass by far previous labeling schemes in terms of cost,

time and straightforwardness, and appeared to us as potentially attractive for developing general procedures for labeling fatty acids in  $^{17}\text{O}$  and  $^{18}\text{O}$ .

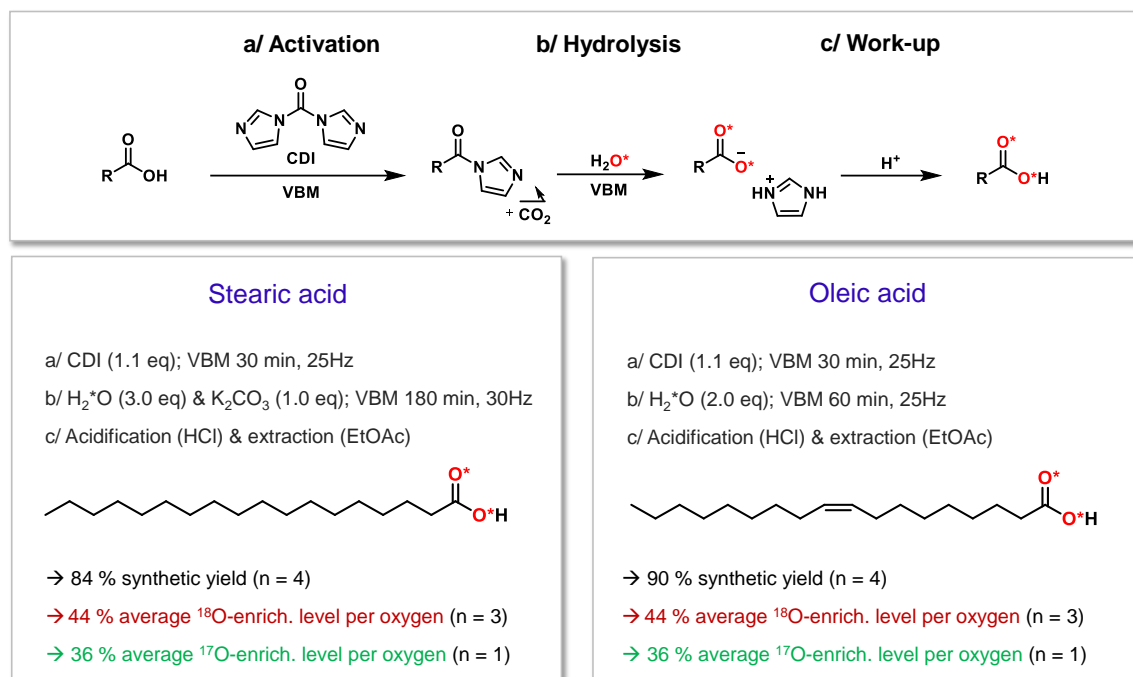
In this manuscript, we demonstrate how mechanochemistry can be used for enriching fatty acids in  $^{17}\text{O}$  or  $^{18}\text{O}$ , in a cost-efficient and user-friendly way. More specifically, the isotopic labeling of stearic acid ( $\text{C}_{17}\text{H}_{35}\text{COOH}$ ) and oleic acid ( $\text{C}_{17}\text{H}_{33}\text{COOH}$ ) will be described, both of these molecules being of major interest in biology and (nano)materials science,<sup>8, 44-48</sup> notably for the synthesis of functional nanoparticles. It will be shown how the synthetic procedures lead to high-purity products with high enrichment yields, and that they can be easily scaled up for the production of up to gram quantities of  $^{17}\text{O}$ - or  $^{18}\text{O}$ -enriched molecules, which is of major importance for being able to use these molecules in standard (nano)materials synthesis protocols. The added-value of having access to the  $^{17}\text{O}$ -labeled molecules for understanding the structure of complex materials systems will then be demonstrated for two related systems: (i) Zn-oleate, a metal soap which is of interest notably in art-preservation sciences<sup>49-51</sup> and for the synthesis of quantum-dots,<sup>52-53</sup> but for which no crystal structure has yet been reported, and (ii) ZnO nanoparticles functionalized by oleic acid, which have been studied in fields like toxicology and pharmacy (e.g. sunscreens),<sup>45, 54-55</sup> art (e.g. oil paints),<sup>44, 56-57</sup> as well as for the elaboration of nanocomposite materials,<sup>58</sup> but for which no direct experimental evidence into the binding mode of the fatty acid on the nanoparticle surface had been provided so far. We will show here how thanks to these new isotopic labeling schemes, high resolution  $^{17}\text{O}$  NMR experiments can be performed, which provide unprecedented insight into the structure and reactivity of these materials, including after UV-irradiation.

## Results and discussion

### 1) Isotopic labeling of oleic and stearic acids using mechanochemistry

In order to label the carboxylic functions of stearic and oleic acid, the synthetic strategy we used consisted in performing two mechanochemical reactions back-to-back, namely (i) the activation of the carboxylic function using 1,1'-carbonyl-diimidazole (CDI),<sup>59</sup> and (ii) the hydrolysis of the acyl-imidazole intermediate with enriched  $\text{H}_2^{17}\text{O}$  (Scheme 1).<sup>42</sup>

**Scheme 1.** General synthetic conditions for the  $^{17}\text{O}$  and  $^{18}\text{O}$  labeling of stearic and oleic acids, when performing the labeling by vibrating ball-milling (VBM) in a mixer mill on “small scale” quantities.



<sup>a</sup> Synthetic yields, enrichment yields and enrichment levels for each molecule are provided (n indicating the number of repetitions of each experiment; see supporting information for complete details and error bars). This synthetic procedure leads to the predominant labeling of one oxygen per carboxylic group, but with both O atoms having the same probability to be enriched in  $^{18}\text{O}$  (which is why they are both highlighted in red in this figure).

Experiments were initially tested on small quantities of material, with less than 100 mg of fatty acid introduced in the 10 mL jar containing two beads. The activation step was performed in presence of a small excess of CDI (1.1 eq), and followed by IR spectroscopy, by looking at the shift in the C=O stretching frequency (see supporting information, Figures B1S1 and B3S1). For both molecules, it was found that 30 minutes were sufficient for this reaction to be complete. The conditions for hydrolysis, however, significantly differed from one molecule to the other, and required optimization to achieve the best yield and enrichment level. Oxygen-18 labeled water was used for these optimizations, due to its lower cost (1 g of 97%  $^{18}\text{O}$ -enriched water costs ~ 80-100 €). The extent of hydrolysis was monitored by IR spectroscopy (by looking at the disappearance of the C=O stretching band of the acyl-imidazole intermediate), and confirmed by mass spectrometry analyses of the hydrolyzed product. In the case of oleic acid, the complete hydrolysis could be performed by ball-milling in just 1 hour, in presence of 2 equivalents of water (see supporting information Figure B3S1). In contrast, in the case of stearic acid, complete hydrolysis required increasing the milling time and frequency, as well as adding 1 equivalent of base,  $\text{K}_2\text{CO}_3$  (see supporting information, Figure B1S1 and Table B1S1). Such a difference in reactivity between both molecules comes from the double bond in oleic acid, which affects the physical-chemical properties of the reaction medium. Indeed, after activation, the oleic acid-derived acyl-imidazole has a pasty texture, while the stearic acid derived one is more powdery, which could explain why the hydrolysis step is more straightforward in the former case. For stearic acid, the addition of  $\text{K}_2\text{CO}_3$  to the reaction medium was found to

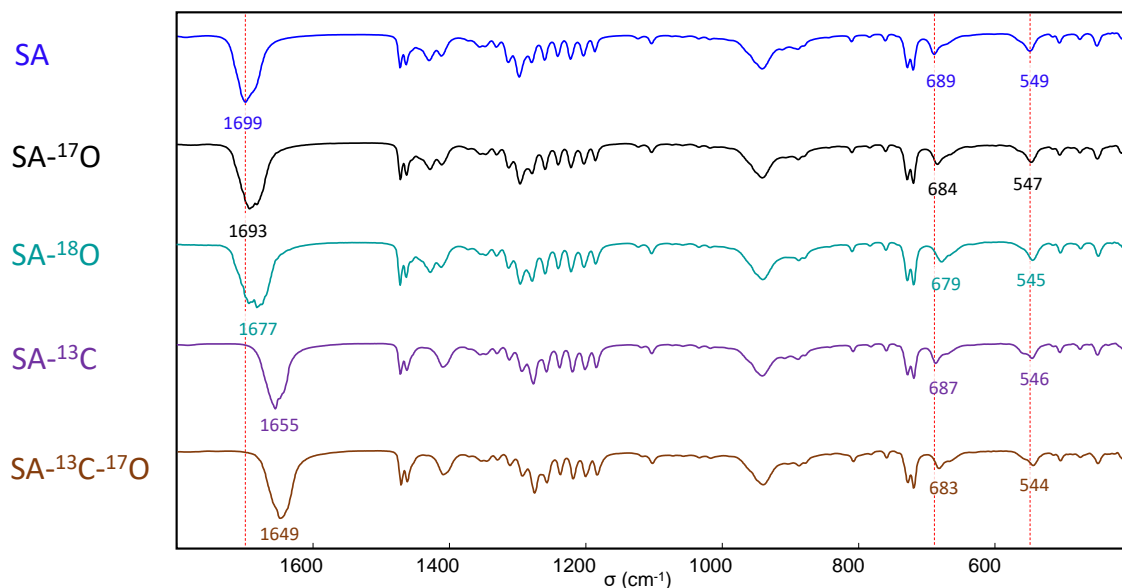
be necessary to accelerate the hydrolysis step, this base favoring the formation of  $\text{H}^*\text{O}^-$  ions in the milling medium, which will be more reactive towards the acyl-imidazole. After hydrolysis, the labeled molecules were then isolated with very good synthetic yields (all  $\geq 84\%$ ).

Oxygen-17 and oxygen-18 enriched oleic and stearic acids were extensively characterized by  $^1\text{H}$  and  $^{13}\text{C}$  solution NMR, LC-MS and mass spectrometry, as well as IR spectroscopy, in order to determine their purity and enrichment level, and to gain detailed insight into some of their spectroscopic features. In all cases, the  $^1\text{H}$  NMR spectra of the isolated products were consistent with those of the starting molecules (see supporting information, Figures B1S4 and B1S10 for stearic acid, and Figures B3S4 and B3S9 for oleic acid). Moreover, mass spectra demonstrate that, as expected, the carboxylic function is predominantly labeled on one of the two oxygen positions, the main molecular peak being shifted by one or two m/z units upon  $^{17}\text{O}$  or  $^{18}\text{O}$  labeling, respectively (see supporting information, Figures B1S2 and B1S8 for stearic acid, and Figures B3S2 and B3S7 for oleic acid). This was further confirmed by  $^{13}\text{C}$  solution NMR analyses of labeled molecules, for which only one main resonance appears in the carboxylic acid region of the spectra, which is shielded by ~ 0.025 ppm in comparison to the non-labeled precursor, and corresponds to a  $-\text{C}^{16}\text{O}^{16}\text{OH}$  head-group (see supporting information, Figures B1S7 and B3S6). In all cases, high enrichment levels were achieved, with an average enrichment per carboxylic oxygen of ~ 44% for the  $^{18}\text{O}$  labeled molecules (when starting from 97%  $^{18}\text{O}$ -enriched  $\text{H}_2^{18}\text{O}$ ), and ~ 36% (when starting from 90%  $^{17}\text{O}$ -enriched  $\text{H}_2^{17}\text{O}$ ).

The labeling of the carboxylic functions in  $^{17}\text{O}$  or  $^{18}\text{O}$  is particularly advantageous for the *direct* assignment of several IR vibrations associated to the carboxylic group. This is illustrated in Figure 1a in the case of stearic acid (top 3 spectra). For this molecule, the most significant shifts after isotopic labeling concern the vibration bands at  $\sim 1699$ , 689 and  $549\text{ cm}^{-1}$ , which decrease by  $\sim 6$ ,  $\sim 5$  and  $\sim 2\text{ cm}^{-1}$ , respectively, after replacement of one of the two carboxylic  $^{16}\text{O}$  atoms by an  $^{17}\text{O}$ , the shifts being even more pronounced in the case of  $^{18}\text{O}$ -labeling. These vibrations correspond to C=O stretching (at  $1699\text{ cm}^{-1}$ ),  $\text{CO}_2$  bending/deformation (at  $689\text{ cm}^{-1}$ ), and  $\text{CO}_2$  wagging modes (at  $549\text{ cm}^{-1}$ ), respec-

tively.<sup>50, 60-62</sup> Such straightforward identification of carboxylic vibration frequencies following isotopic substitutions on the oxygen sites is highly complementary to experimental analyses on molecules enriched in  $^{13}\text{C}$ . Indeed, the extent of isotopic shifts varies depending on which carboxylic atom(s) has been enriched (C or O), as illustrated in Figure 1a (bottom spectra) for a commercial stearic acid molecule labeled in  $^{13}\text{C}$  on the carboxylic group. For example, the main C=O stretching band is now centered at  $1655\text{ cm}^{-1}$ , and further shifts by  $6\text{ cm}^{-1}$  after  $^{17}\text{O}$  labeling. Overall, this means that the oxygen-labeling of fatty acids offers new possibilities to confirm IR spectral assignments, and/or help resolve vibration bands which may overlap.

### a/ IR analyses of enriched stearic acid



### b/ $^{17}\text{O}$ MAS NMR of enriched stearic and oleic acids

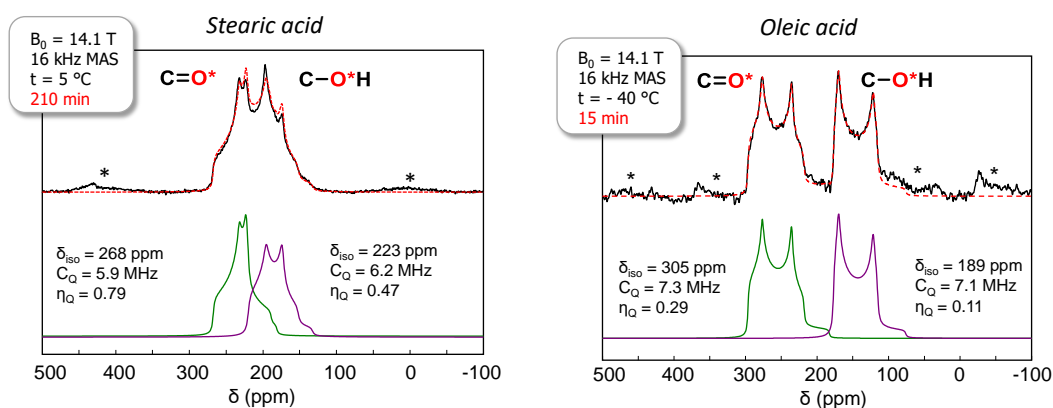


**Figure 1.** a/ IR spectra of stearic acid (SA), at natural abundance (dark blue spectrum), enriched in  $^{17}\text{O}$  (average  $^{17}\text{O}$ -labeling  $\sim 36\%$ ; black spectrum), enriched in  $^{18}\text{O}$  (average  $^{18}\text{O}$ -labeling  $\sim 44\%$ ; light blue spectrum), enriched in  $^{13}\text{C}$  on the carboxylic group ( $^{13}\text{C}$  labeling  $\sim 99\%$ ; purple spectrum), and enriched in  $^{13}\text{C}$  and  $^{17}\text{O}$  on the carboxylic group ( $^{13}\text{C}$  labeling  $\sim 99\%$  and average  $^{17}\text{O}$ -labeling  $\sim 39\%$ ; brown spectrum).<sup>63</sup> b/  $^{17}\text{O}$  MAS NMR spectra of  $^{17}\text{O}$ -labeled stearic acid (left) and oleic acid (right), together with the fit (dashed red line), showing the contributions from the “C=O\*” and “C-O\*H”-like environments (green and purple spectra). The average  $^{17}\text{O}$ -labeling of the carboxylic groups in the molecules studied here by NMR was  $\sim 36\%$  for stearic acid and  $\sim 19\%$  for oleic acid. “\*” symbols correspond to spinning sidebands.

Molecules enriched in oxygen-17 were also analyzed by  $^{17}\text{O}$  magic-angle spinning (MAS) solid state NMR (Figure 1b). In the case of oleic acid, measurements were performed at low temperature, as the melting point of the molecule is  $\sim 13^\circ\text{C}$ . Although predominant contributions from “ $\text{C}=\text{O}$ ” and “ $\text{C}-\text{OH}$ ” like environments can be clearly distinguished on the MAS NMR spectra of both molecules,<sup>27, 64</sup> a more significant overlap of these resonances is observed in the case of stearic acid. Given that fatty acids have been shown to crystallize with the polar head-chains forming H-bonded dimers,<sup>65–69</sup> such differences are likely to arise from discrepancies in the localization of the OH hydrogen atoms,<sup>68</sup> and hence in relative energy of the two interconverting tautomeric forms, as this can significantly impact  $^{17}\text{O}$  MAS NMR spectra.<sup>70–71</sup> From a more practical point of view, both of these  $^{17}\text{O}$  NMR spectra could be recorded with very good signal-to-noise ratio in short time (less than 4 hours on a 600 MHz NMR instrument), making these enriched molecules highly promising precursors for helping elucidate the structure of more complex molecular and materials systems.

Having demonstrated the purity and high-enrichment level of the oleic and stearic acid molecules labeled by ball-milling, and their interest for fine structural analyses using IR and  $^{17}\text{O}$  NMR spectroscopies, the obvious next step was to look into the scale-up of the syntheses. Indeed, in order to be able to use  $^{17}\text{O}$ - (or  $^{18}\text{O}$ -) enriched fatty acids in “routine” molecular and materials science applications, it is necessary to have access to  $\sim$  gram quantities of enriched compounds. In both cases, given that the activation step leads to the release of  $\text{CO}_2$ , larger volume milling jars were used, to avoid any excessive build-up of internal pressure inside the reactors. Scale-up experiments were first tested in a mixer mill using 50 mL milling jars. For oleic acid, this allowed the production of  $\sim 1$  g of  $^{17}\text{O}$ -enriched oleic acid with very good synthetic yield ( $\sim 92\%$ ) and enrichment level (average  $^{17}\text{O}$ -enrichment per carboxylic oxygen  $\sim 37\%$ ) in less than 4 hours (work-up included). In the case of stearic acid, scale-up experiments were also attempted in a mixer mill under similar conditions, but the hydrolysis step was once more found to be problematic, despite the presence of additional  $\text{K}_2\text{CO}_3$ . Even by decreasing the amount of sample to  $\sim 500$  mg, or by modifying the number of beads used during the milling, the hydrolysis remained incomplete after 4 hours, according to IR and mass spectrometry analyses. In order to change the type of mixing of the reaction medium during the hydrolysis, the enrichment of stearic acid was then studied on a planetary mill, using 20 mL jars. Here, after careful optimization of the milling parameters (see supporting information, Table B1S2), it was possible to reduce the hydrolysis time to just 1 hour, and produce  $\sim 500$  mg of  $^{18}\text{O}$ -enriched stearic acid with very good synthetic yield ( $\sim 95\%$ ) and enrichment level (average  $^{18}\text{O}$ -enrichment per carboxylic oxygen  $\sim 46\%$ ). To the best of our knowledge, it is the first time that the enrichment of oleic and stearic acids in  $^{17}\text{O}$  or  $^{18}\text{O}$  is reported on such a large scale and with such a high efficiency, both in terms of time and cost. To be more specific, in the case of oleic acid, the production of  $\sim 1$  g of  $^{17}\text{O}$ -enriched molecule could be achieved in just half-a-day of experimental time, and required only  $\sim 150$   $\mu\text{L}$  of  $\text{H}_2^*\text{O}$  (which corresponds to a cost of less than 300 € if 90%-enriched  $\text{H}_2^{17}\text{O}$  is used). It is worth noting that these oxygen

isotopic enrichments were found to be stable over time: the enrichment levels determined by mass-spectrometry for  $^{17}\text{O}$ - or  $^{18}\text{O}$ - enriched samples which had been stored for one year on the bench or in the fridge led to sensibly similar results (see supporting information, Tables B1S3 and B3S1).

## 2) Advanced structural analyses of metal soaps and functionalized nanoparticles

The straightforward and inexpensive  $^{17}\text{O}$  and  $^{18}\text{O}$  labeling of fatty acids described above naturally opens the way to using vibrational spectroscopies and  $^{17}\text{O}$  NMR for studying in detail the structure of fatty-acid containing phases. Here, we set our focus on two related systems, namely Zn-oleate and ZnO nanoparticles functionalized using oleic acid, because in both cases, despite the numerous investigations reported so far, detailed structural information was missing, including the mode of binding of the fatty acid to zinc ions.

### *2a- Zn-oleate coordination polymer*

A crystalline Zn-oleate phase enriched in  $^{17}\text{O}$  was synthesized, starting from  $^{17}\text{O}$ -enriched oleic acid, and following a new synthetic procedure based on mechanochemistry (see supporting information, section C1). The IR spectra of this enriched phase and its non-labeled analogue were first analyzed in detail and compared. This allowed (i) assigning (or re-assigning) the carboxylate vibration frequencies, and (ii) demonstrating the presence of at least two oleate environments in the crystal structure, because of the observation of 2 resolved  $\nu_a(\text{COO})$  bands at 1546 and 1525  $\text{cm}^{-1}$  (see supporting information, Figure C3S1 and section C3-b). The difference in frequency between the  $\nu_a(\text{COO})$  and  $\nu_s(\text{COO})$  stretching modes was found to be consistent with a bidentate coordination mode of the carboxylate groups.<sup>72</sup> Moreover, the low-frequency band at 550  $\text{cm}^{-1}$  (carboxylate rocking mode) was observed at a wavenumber close to the one reported for anhydrous Zn-acetate and Zn-stearate, in which the carboxylate group adopts a bridging bidentate coordination mode. Hence, it appears that the carboxylate functions in Zn oleate also adopts a similar binding mode, with each oxygen of a given carboxylate being bound to a different  $\text{Zn}^{2+}$  cation.<sup>73</sup> This is in line with what has been observed for other Zn-soap phases for which X-ray structures are available.<sup>74</sup>

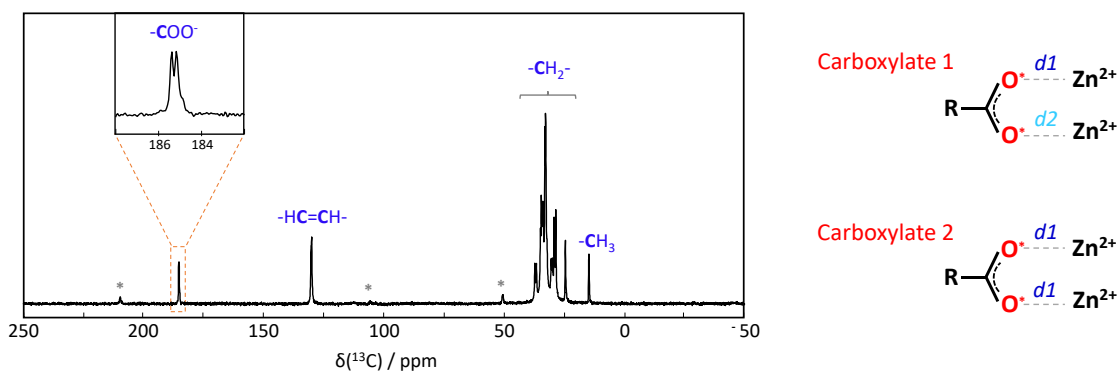
High resolution  $^{13}\text{C}$  and  $^{17}\text{O}$  MAS NMR experiments were then performed, in order to gain deeper insight into the carboxylate environments of Zn-oleate. First, in  $^{13}\text{C}$  NMR, two carboxylate resonances of equal intensity were observed (separated by only  $\sim 0.2$  ppm; Figure 2a), as well as two  $\alpha\text{-CH}_2$  resonances (Figure C2S2), which confirms that two non-equivalent carboxylate ligands are present in the crystal structure.<sup>75</sup> Second, in  $^{17}\text{O}$  NMR, two different oxygen environments could be clearly resolved by performing a 3QMAS experiment (triple quantum magic angle spinning). These were found to be in a relative proportion of 3:1, with a difference in  $^{17}\text{O}$  isotropic chemical shifts of  $\sim 6$  ppm (Figures 2b and C3S2). Such observations could be consistent with 3 of the oxygen atoms of the two inequivalent carboxylates having similar binding modes to  $\text{Zn}^{2+}$ , and one being slightly different, possibly because of a change in the Zn...O distance, as schematized in Figure 2.

In order to confirm this hypothesis, a computational study was performed on Zn-carboxylate phases for which a crystal structure had already been reported, and in which the  $\text{Zn}^{2+}$  also adopts a bridging bidentate coordination (i.e. with each carboxylate oxygen linked to one  $\text{Zn}^{2+}$  ion). For these phases, *ab initio* calculations of the  $^{17}\text{O}$  NMR parameters were performed using the GIPAW DFT method (Gauge-Including Projector Augmented Wave – Density Functional Theory),<sup>76-77</sup> and calculated values were confronted to the local geometry around the oxygen. As shown in supporting information (section C3-d), this enabled to demonstrate a strong dependence between the isotropic chemical shift of  $^{17}\text{O}$  and the Zn...O distance. Indeed,  $\delta_{\text{iso}}(^{17}\text{O})$  values were found to span over  $\sim 40$  ppm, with the isotropic shift increasing as the Zn...O distance increased. More specifically, based on the calculations, a change as small as  $0.08 \text{ \AA}$  in this distance could lead to an increase by  $\sim 40$  ppm in  $\delta_{\text{iso}}(^{17}\text{O})$ ! No other relationship could be found between the local structure around oxygen and the calculated  $\delta_{\text{iso}}(^{17}\text{O})$  values. This implies that the  $\sim 6$  ppm difference observed between the two sets of  $^{17}\text{O}$  resonances in Zn-oleate must be due to a

very small difference in Zn...O distances, which can be estimated to  $\sim 0.01 \text{ \AA}$  on the basis of the GIPAW-DFT calculations.

Such detailed level of insight had never been reached so far for Zn-oleate, and could only be achieved by looking at  $^{17}\text{O}$ , thanks to the very high  $^{17}\text{O}$ -isotopic labeling of oleic acid. Indeed, more conventional  $^{13}\text{C}$  solid state NMR analyses could not have provided such level of information, because (i) they inform on the number of inequivalent carboxylate ligands (but not on the binding modes of the individual carboxylate oxygen atoms), and (ii) the range of variation of  $^{13}\text{C}$  NMR parameters in Zn-carboxylates is more limited compared to oxygen (with notably isotropic shifts spanning only over  $\sim 10$  ppm for  $^{13}\text{C}$ , compared to 40 ppm for  $^{17}\text{O}$ ), meaning that it is less sensitive to geometrical changes in the coordination (see supporting information section C3-d). Hence, on a more general perspective, similar high-resolution  $^{17}\text{O}$  NMR studies would be worth performing on other metal soaps of unknown structure.

a/  $^{13}\text{C}$  CPMAS



b/  $^{17}\text{O}$  3QMAS

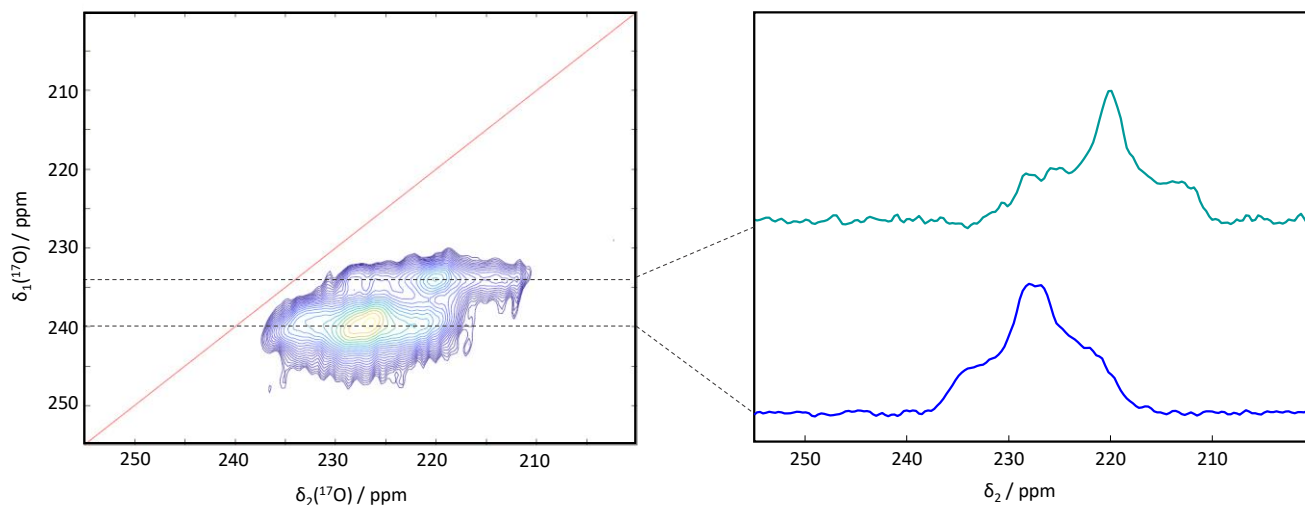


**Figure 2.** a/  $^{13}\text{C}$  CPMAS NMR spectrum of  $^{17}\text{O}$ -labeled Zn-oleate ( $B_0 = 14.1 \text{ T}$ ,  $\nu_r = 12 \text{ kHz}$ ,  $\text{CT} = 8 \text{ ms}$ ), showing the presence of 2 inequivalent carboxylate environments (see Figure C2S2 in supporting information, for an expansion of the  $\alpha\text{-CH}_2$  region).<sup>75</sup> b/ Ultra-high field  $^{17}\text{O}$  3QMAS NMR spectrum ( $B_0 = 35.2 \text{ T}$ ,  $\nu_r = 18 \text{ kHz}$ ), and resolved sites (right). A possible fit of the resolved  $^{17}\text{O}$  sites is proposed in supporting information (Figure C3S2, supporting information).



## 2b- ZnO nanoparticles functionalized using oleic acid

Oleic acid being one of the main surfactant molecules involved in the synthesis of metal and metal oxide nanoparticles,<sup>78-82</sup> the obvious next step was to show how using  $^{17}\text{O}$ -enriched species can help shed light on their mode of attachment and reactivity at the surface of NPs. Here, we set our focus on functionalized ZnO NPs. Indeed, previous investigations based on XRD, TEM, IR and/or XPS analyses had shown that oleic acid is present at the surface of ZnO nanoparticles and can influence nanoparticle sizes and shapes, but with no clear experimental insight into its exact mode of binding, nor on how it can be affected by exposure to heat or UV light.<sup>83-86</sup>

A “post-grafting” synthetic approach was used here to prepare oleic-acid capped ZnO NPs. It consisted in first synthesizing the ZnO nanoparticles, which were obtained as nanorods, by reacting Zn-acetate dihydrate with KOH in methanol at 60°C overnight.<sup>87-88</sup> Then, the surface of the nanoparticles was functionalized by oleic acid, using either  $^{17}\text{O}$ -labeled oleic acid, prepared according to the “scale-up” protocol described above, or non-labeled oleic acid, used here for the preparation of “control” samples. Finally, the grafted particles were washed, dried under vacuum, and characterized by X-ray diffraction, TGA, TEM, IR and multinuclear solid state NMR spectroscopies ( $^1\text{H}$ ,  $^{13}\text{C}$  and  $^{17}\text{O}$  NMR) (see supporting information).

Based on X-ray diffraction and TEM analyses, the size and shape of the ZnO nanorods was not altered by the surface functionalization process (Figure 3a,b). X-ray diffraction powder patterns displayed the characteristic features expected for nanorods, with a sharper peak at 34.4° in 2 $\theta$ ,<sup>87</sup> and no new diffraction peaks at lower angles. The latter point was important to verify, as it confirmed that no “dissolution-recrystallization” process had taken place during the grafting, and hence that no Zn-oleate by-product had formed (see Supporting information, Figure D1S4, for direct comparison with Zn-oleate). Based on TGA, the average grafting density was estimated to  $\sim 2$  molecules per nm<sup>2</sup>. The presence of oleic acid at the surface of the nanorods is detectable by IR spectroscopy, through the appearance of C-H stretching vibrations around 2900 cm<sup>-1</sup> (Figure 3c, blue and green spectra). The aliphatic carbon peaks of oleic acid could also be observed in  $^{13}\text{C}$  solid state NMR, with the  $^{13}\text{C}$  resonance at  $\sim 130$  ppm corresponding to the carbons of the alkene bond, and those between 10 and 45 ppm to the carbons belonging to CH<sub>2</sub> and CH<sub>3</sub> groups (Figure 3d, blue and green spectra).

To understand the mode of binding of oleic acid at the ZnO surface, the spectroscopic signatures of the carboxylic group were analyzed. In IR spectroscopy, the broad vibration bands observed in the C=O stretching region were found at similar positions before and after functionalization of the nanorods, *i.e.* centered around 1430 and 1565 cm<sup>-1</sup>. For the starting ZnO nanorods, the observation of these broad bands can be explained by the presence of residual acetate and carbonate ions at the surface of the particles, as confirmed by  $^{13}\text{C}$  solid state NMR, with the distinct  $^{13}\text{C}$  resonances at 180.5 and 21.9 ppm (acetate) and at 166.2 ppm (carbonate) (Figure 3d, black spectrum). It is worth noting that previous studies on ZnO nanoparticles have reported the presence of these anions, for syntheses carried out using

Zn-acetate as precursor,<sup>88-89</sup> or following exposure of ZnO nanoparticles to CO<sub>2</sub> (including at atmospherically relevant pressures).<sup>90-91</sup> For the OA-functionalized nanorods, the lack of significant shift in the C=O stretching region and the absence of a new band around 1700 cm<sup>-1</sup> (which is characteristic of the acidic form of oleic acid), suggests that it is mainly the oleate which is present at the surface of the particles (see Figure D1S5 for a comparison of the IR spectra of Zn-oleate, oleic acid, and the functionalized nanorods).<sup>10,11,61</sup>

Because previous works on oleic acid-grafted ZnO nanoparticles had proposed that either protonated or deprotonated forms of oleic acid can attach to the surface of the nanoparticles,<sup>86,92-93</sup> additional solid-state NMR analyses were performed. In  $^{13}\text{C}$  solid state NMR, only one broad resonance was observed in the high-frequency region of the functionalized nanoparticles, centered at  $\sim 181.1$  ppm (Figure 3d, blue and green spectra). This  $^{13}\text{C}$  resonance is broader than those of the rest of the organic chain, as expected for a grafting process occurring through the carboxylic moiety.<sup>13,94</sup> Although its chemical shift was found to be closer to the one observed for pure oleic acid (carboxylic resonance is centered at  $\sim 181.4$  ppm, as measured by  $^{13}\text{C}$  CPMAS NMR while regulating temperature at -20°C),<sup>95-96</sup> than for Zn-oleate (carboxylate resonances centered at  $\sim 185.3$  ppm), it is still compatible with a deprotonated function, because the  $^{13}\text{C}$  chemical shift range of grafted carboxylates can vary depending on their binding mode and distance to the surface of nanoparticles.<sup>11</sup> As a matter of fact, when recording a 2D  $^1\text{H}$ - $^{13}\text{C}$  heteronuclear correlation experiment, the  $^{13}\text{C}$  resonance at 181.1 ppm was not found to correlate with any  $^1\text{H}$  resonances characteristic of acidic protons, which are generally expected above 10 ppm. Moreover, no distinct  $^1\text{H}$  carboxylic resonance could be observed in  $^1\text{H}$  MAS NMR, even when performing the analyses at temperatures as low as -100°C (see supporting information, Figure D1S6). Therefore, these complementary NMR characterizations also tend to confirm that it is mainly the oleate form which is present at the surface of the nanoparticles.

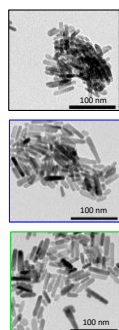
In view of reaching deeper insight into the mode of binding of the fatty acid at the surface of ZnO,  $^{17}\text{O}$  solid state NMR analyses were carried out. As shown in Figure 3e (green spectrum), the  $^{17}\text{O}$  NMR spectrum of the grafted nanoparticles presents one main broad signal, centered at  $\sim 200$  ppm (at 14.1 T). This signal is not observed for the starting nanoparticles, nor for those which were reacted using non-labeled oleic acid, and can therefore be assigned to the enriched carboxylic function of oleic acid. The spectrum was obtained overnight with a good signal-to-noise ratio at 14.1 T, which is all the more noteworthy that the analysis was performed on just  $\sim 35$  mg of sample. Indeed, this corresponds to only  $\sim 0.1$  mg of  $^{17}\text{O}$  from the oleic acid head-group, based on the initial enrichment of the molecule used in the grafting and on the grafting density determined from TGA analyses of the functionalized nanoparticles. Other weaker resonances were also observed on the  $^{17}\text{O}$  NMR spectrum, at  $\sim -18$  ppm (natural abundance signal corresponding to the core of the ZnO nanoparticles)<sup>97-98</sup> and at  $\sim 380$  ppm (natural abundance signal of the zirconia rotor



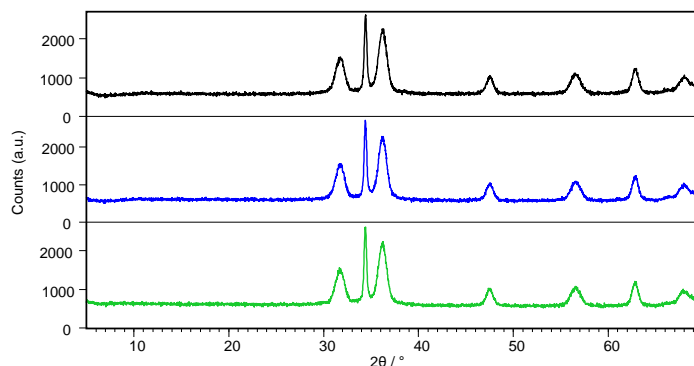
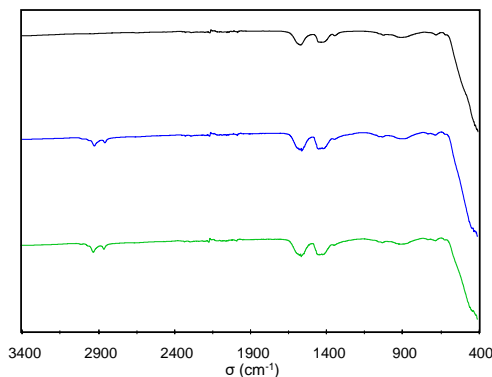
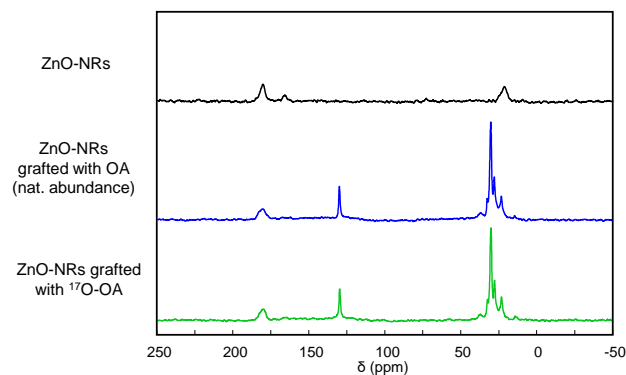
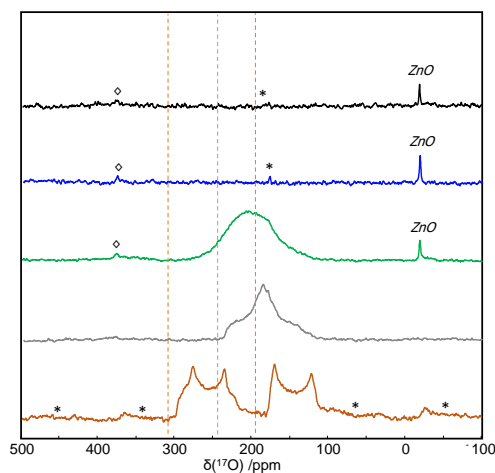
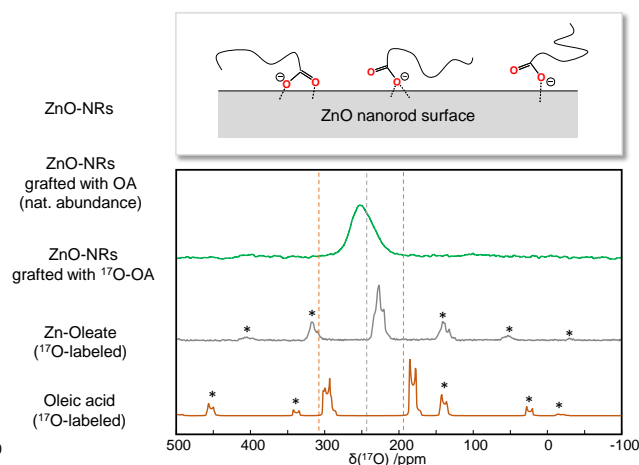
used for the analyses), which were also present on the spectra of the non-grafted nanoparticles and those grafted using non-labeled oleic acid (Figure 3e, black and blue spectra).

The  $^{17}\text{O}$  NMR signal centered at  $\sim 200$  ppm falls in the range expected for carboxylic acids and carboxylates,<sup>26,99</sup> as shown in Figure 3e when comparing it to oleic acid and Zn-oleate (brown and grey spectra). However, when cooling the sample down to  $-100^\circ\text{C}$ , only a slight shift and broadening of the  $^{17}\text{O}$  NMR signal was observed, but no splitting into distinct C=O and C-OH contributions as for oleic acid (see supporting information, Figure D1S7). Moreover, when heating up to  $+60^\circ\text{C}$ , the signal is slightly narrower and more symmetric (as expected if the molecules become somewhat more mobile at the nanoparticle surface), but its maximum position increases by less than 15 ppm, thereby remaining very distinct to that of liquid oleic acid. This could reflect the fact that the grafted OA species remain rel-

atively well attached to the ZnO surface even at high temperatures, through coordination bonds between  $\text{Zn}^{2+}$  and the carboxylate, and that there are only few more weakly bound species interacting through hydrogen bonding (as may have been expected upon grafting of the oleic acid form). Overall, these variable-temperature  $^{17}\text{O}$  NMR analyses also appear to be consistent with the predominance of oleate anions at the surface of the nanoparticles. However, because of the wide range of chemical shifts covered by this  $^{17}\text{O}$  signal, which spreads over  $\sim 180$  ppm at 14.1 T (between  $\sim 110$  and 290 ppm), additional characterizations were performed at ultra-high magnetic field ( $B_0 = 35.2$  T), in order to try to achieve better resolution and gain further insight into the grafting mode. Indeed,  $^{17}\text{O}$  being a quadrupolar nucleus, going to higher fields decreases significantly the broadening caused by the quadrupolar interaction, the second-order quadrupolar broadening being inversely proportional to  $B_0$ .

**a/ TEM**

ZnO-NRs

ZnO-NRs grafted with OA  
(nat. abundance)ZnO-NRs grafted with  $^{17}\text{O}$ -OA**b/ X-ray diffraction****c/ IR spectroscopy****d/  $^{13}\text{C}$  CPMAS NMR****e/  $^{17}\text{O}$  MAS NMR (14.1 T)****f/  $^{17}\text{O}$  MAS NMR (35.2 T)**

**Figure 3.** a-f/ TEM, XRD, IR,  $^{13}\text{C}$  CPMAS NMR and  $^{17}\text{O}$  MAS NMR characterization of bare ZnO nanorods (black), nanorods grafted with non-labeled OA (blue) and nanorods grafted with  $^{17}\text{O}$ -labeled OA (green). For the  $^{17}\text{O}$  MAS NMR analyses, the spectra of  $^{17}\text{O}$ -labeled Zn oleate (grey) and oleic acid (brown) are also shown for comparison. (At 14.1T, it is the same experimental  $^{17}\text{O}$  NMR spectrum of OA as shown in Figure 1, while at 35.2T, it is its simulation for a 32 kHz spinning speed, as was used for the nanoparticles at this field, and estimating the CSA parameters from GIPAW-DFT calculations). For the  $^{17}\text{O}$ -OA grafted nanorods, the lack of natural abundance ZnO signal at 35.2T (f, green spectrum) is ascribed to the difference in acquisition conditions used in comparison to the study at 14.1T (e, green spectrum). All NMR acquisition parameters can be found in supporting information (Tables A3S1 and A3S2). “\*” symbols correspond to spinning sidebands, and “◊” symbols to the natural abundance signal of the zirconia rotor. The dashed vertical lines indicate the isotropic peak positions of the C=O and C-OH resonances of oleic acid (brown) and the high frequency carboxylate resonance of Zn-oleate (grey). A schematic representation of possible grafting modes of OA on the ZnO surface is also shown in f/ (using a simplified representation of the aliphatic chain, without depicting the C=C double bond).

At 35.2 T, the main resonance spreads over  $\sim 90$  ppm only (between  $\sim 200$  and  $290$  ppm), and is now shifted at higher frequency  $\sim 250$  ppm, as expected considering the field dependence of the maximum peak-position of solid state NMR spectra of quadrupolar nuclei (Figure 3f). Although no additional resolution could be obtained, this 1D  $^{17}\text{O}$  MAS NMR spectrum nevertheless shows that there are several oxygen local environments at the surface of the nanoparticles, because the linewidth expected for  $^{17}\text{O}$  resonances from carboxylic or carboxylate oxygen atoms is less than  $20$  ppm at  $35.2$  T. Moreover, on the spectrum recorded at this field, the  $^{17}\text{O}$  peak maximum position is very clearly positioned at higher frequencies compared to the Zn-oleate model compound. This demonstrates that the main mode of binding of oleate to the ZnO nanorod surface is different compared to Zn-oleate, meaning that there are very few oleate ligands coordinated through a bidentate bridging mode to the surface  $\text{Zn}^{2+}$  ions. Considering the results of the DFT calculations reported in Figure C3S3, the higher frequency of the maximum peak position in the functionalized nanorods may suggest that Zn...O distances between the oleate and the nanoparticle surface are not only more distributed but also on average slightly longer than in crystalline Zn-oleate. More specifically, an average increase in distance  $\sim 0.04$  Å can be proposed.

Taken together, the observations made by IR and variable-temperature  $^1\text{H}$  and  $^{17}\text{O}$  NMR suggest the predominance of oleate species at the surface of the nanoparticles. Moreover, the  $^{13}\text{C}$  NMR and ultra-high field  $^{17}\text{O}$  NMR spectra point to the attachment of the oleates through the carboxylate function, with a heterogeneity of local environments at the surface of the nanorods. The aliphatic carbon atoms interact much more weakly with the surface, as shown by the sharper resonances in  $^{13}\text{C}$  NMR,<sup>94</sup> and by the similar chemical shifts as for liquid oleic acid (see supporting information, Figure D1S8). As a matter of fact, the mobility of the aliphatic chains only significantly decreases below  $-45^\circ\text{C}$ , as shown by the variable-temperature  $^1\text{H}$  NMR data (see supporting information, Figure D1S6). Considering that it is the acidic form of oleic acid which was initially introduced in THF for the post-functionalization procedure used here, and that the lateral facets of the nanorods (which are parallel to the  $c$  axis) are apolar,<sup>83,100</sup> a direct attachment of oleate species is unlikely. However, it can be proposed that the grafting occurs by exchange with acetate ligands initially present at the surface of the nanorods, which would be released in THF under the form of acetic acid upon coordination of the oleate, thereby ensuring the charge balancing.<sup>95</sup> A schematic representation of possible modes of attachment of oleates is given in Figure 3f. While this binding mode to ZnO nanorods was proposed here, it is possible that other synthetic strategies for the functionalization of ZnO

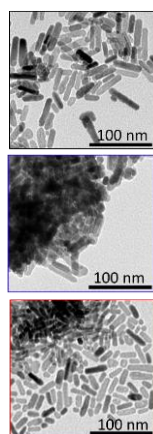
nanoparticles may lead to different binding configurations, depending on the size and shape of the particles, and whether a direct-grafting strategy or post-grafting strategy is used.

Because of the photocatalytic properties of ZnO, we then investigated the stability of the oleate coating upon exposure to UV-vis radiation. More specifically, a batch of grafted nanorods taken in their powdered form was irradiated for 6 hours, after which X-ray diffraction, TEM, IR spectroscopy,  $^{13}\text{C}$  NMR and  $^{17}\text{O}$  NMR analyses were carried out (Figure 4). In order to distinguish the evolutions coming from heating or irradiation, a separate batch of the grafted nanorods was heated at  $60^\circ\text{C}$  in a closed furnace for the same period of time as this temperature was estimated as representative of the heating occurring within the apparatus used for irradiation. Moreover, for comparison purposes, the other two sets of samples described above (*i.e.* bare nanorods and nanorods coated with non-labeled oleic acid), as well as the crystalline Zn-oleate phase, were also exposed to the same treatments (irradiation and heating), and subsequently characterized by the same techniques (see ESI Figures D2S1, D2S2 and D2S3).

While the heating of the non-grafted and grafted ZnO samples at  $60^\circ\text{C}$  for 6h did not lead to noticeable changes in TEM, XRD, IR,  $^{13}\text{C}$  NMR or  $^{17}\text{O}$  NMR (Figure 4, and Figures D2S1 and D2S2), significant differences were observed upon irradiation. First, regarding crystal morphologies, the irradiation step was found to strongly affect the non-grafted nanorods, as shown by TEM (more ill-defined crystal morphologies) and XRD (decrease in the relative intensity of the (002) diffraction peak at  $\sim 34.4^\circ$  in  $2\theta$ ). In contrast, no strong changes in shape and morphology of the grafted nanorods was observed in TEM and XRD after irradiation (Figures 4a and 4b). The OA surface coating thus appears to have had some protective effect for ZnO nanorods under the irradiation conditions used here.

Nevertheless, the grafted molecules do not remain unaffected by the UV-vis treatment, considering the more significant agglomeration of the crystallites observed in TEM (Figure 4a), as well as the results of IR, solid state NMR, and TGA analyses after irradiation. Indeed, TGA data shows that the weight loss due to the combustion of the organic coating is less significant after irradiation (see Figure D2S4 in supporting information), in agreement with the degradation of some of the fatty acid molecules. IR spectroscopy shows a broadening of the carboxylate stretching vibrations after irradiation, as well as a decrease in relative intensity of the CH stretching vibrations (Figure 4c). Such a decrease in the CH bands had also been reported in previous studies of the photodegradation of fatty-acids coated at the surface of ZnO.<sup>101</sup> Changes in the  $^{13}\text{C}$  CPMAS NMR spectra also point to

### a/ TEM

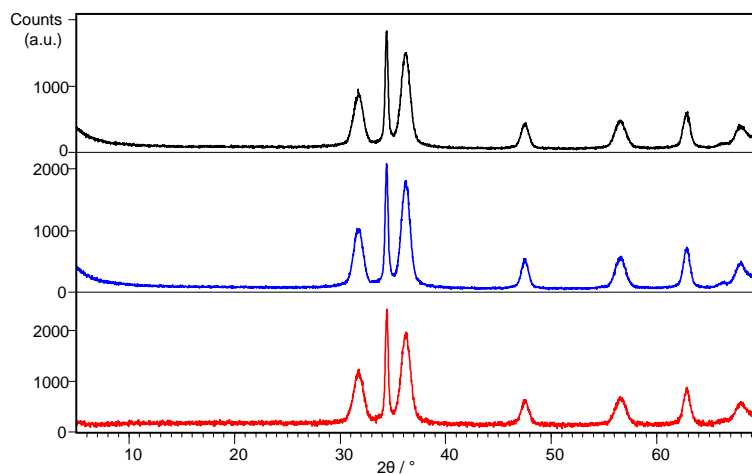


ZnO-NRs grafted  
with  $^{17}\text{O}$ -OA

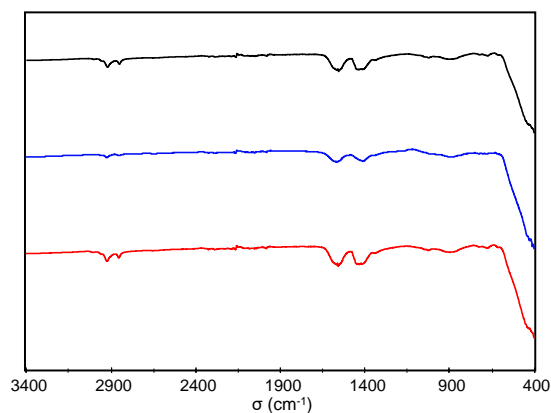
After 6h  
irradiation

After 6h  
heating

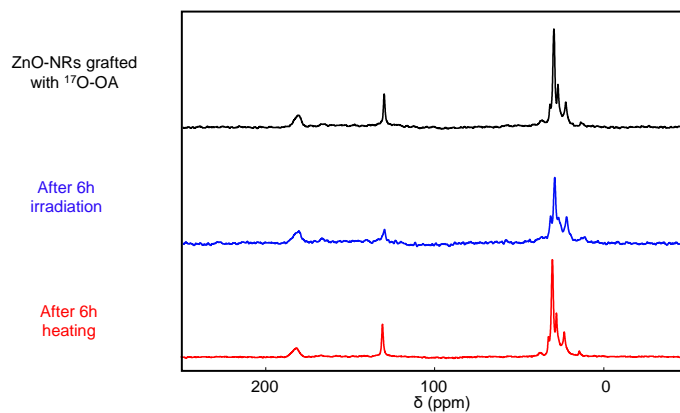
### b/ X-ray diffraction



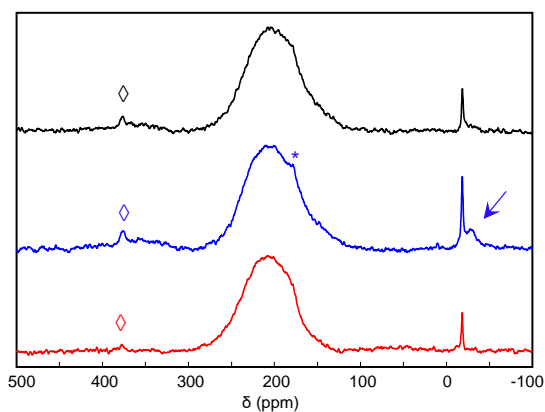
### c/ IR spectroscopy



### d/ $^{13}\text{C}$ CPMAS NMR



### e/ $^{17}\text{O}$ MAS NMR



### f/

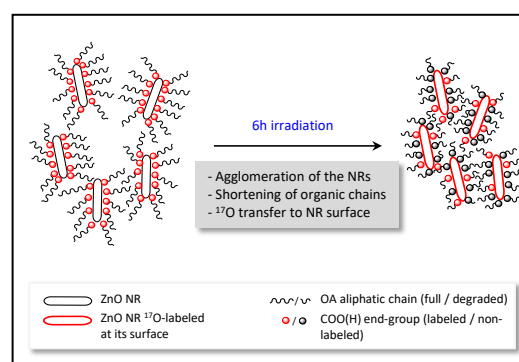


**Figure 4.** a-e/ TEM, XRD,<sup>102</sup> IR,  $^{13}\text{C}$  CPMAS NMR and  $^{17}\text{O}$  MAS NMR characterization of ZnO nanorods functionalized by with  $^{17}\text{O}$ -enriched OA, before (black) and after 6h hours of irradiation (blue) or heat-treatment (red). For the  $^{17}\text{O}$  MAS NMR spectrum recorded after UV irradiation, the blue arrow points to the enriched surface sites. “\*” symbols correspond to spinning sidebands, and “◇” symbols to the natural abundance signal of the zirconia rotor. All NMR acquisition parameters can be found in supporting information (Tables A3S1 and A3S2). f/ Schematic illustration of the different processes occurring upon irradiation of the grafted nanorods.

the degradation of surface oleic acid molecules. Indeed, an overall decrease in signal-to-noise ratio in comparison to the non-irradiated grafted nanorods was observed, together with a reduction in intensity of the  $^{13}\text{C}$  resonances of the aliphatic chain relative to the carboxylate ones, the decrease being more pronounced for the C atoms of the alkene bond (at  $\sim 130$  ppm) than those of the  $\text{CH}_2$  and  $\text{CH}_3$  groups (between 5 and 45 ppm) (Figure 4d). It is worth noting that the changes in IR and NMR signatures of OA observed here appear to be caused by the ZnO nanorods and not the photoreactivity of OA alone, because no variations were observed by IR or  $^{13}\text{C}$  NMR for the Zn-oleate coordination polymer under similar irradiation conditions (see supporting information, Figure D2S3). Taken together, all these observations are in line with previous investigations on the photodecomposition of organic molecules at the surface of ZnO, which can lead to a shortening of the organic chain of fatty acids,<sup>9</sup> and eventually to the formation of  $\text{CO}_2$  and  $\text{H}_2\text{O}$ .<sup>103</sup>

$^{17}\text{O}$  MAS NMR analyses were found to provide further information on the reactions occurring at the surface of the grafted nanorods upon irradiation (Figure 4e). Indeed, while no strong difference was noticed after simple heating, a decrease in the relative intensity of the carboxylic resonances with respect to the signal coming from the ZnO nanoparticles core signal at  $\sim -18$  ppm was observed after irradiation, which is consistent with the photodegradation of part of the organic molecules at the surface of ZnO. More interestingly, a new signal was observed at  $\sim -28$  ppm, which can be assigned to oxygen surface sites, based on previous  $^{17}\text{O}$  NMR studies of ZnO nanorods.<sup>97-98</sup> Considering the small number of O surface sites in comparison to bulk for this size of nanorods, such surface sites are not expected to be readily detectable in absence of isotopic labeling. As a matter of fact, this new signal was found to be absent from the  $^{17}\text{O}$  MAS NMR spectra of the bare nanorods and nanorods grafted with non-labeled OA after 6h irradiation (see supporting information, Figures D2S1 and D2S2). Overall, this shows that these surface oxygen atoms have become enriched in  $^{17}\text{O}$  as a consequence of the irradiation of the grafted  $^{17}\text{O}$ -labeled OA, as schematically illustrated in Figure 4f. To the best of our knowledge, direct experimental evidence of oxygen exchange/transfer processes occurring during the photodecomposition of organic molecules at the surface of ZnO had not been provided so far, and could not have been revealed by other characterization techniques like XPS, IR or photoluminescence spectroscopy. This clearly shows the added value of having synthesized  $^{17}\text{O}$ -enriched molecules for reaching atomic-level insight into the different photocatalytic reactions at the surface of ZnO. More generally speaking, considering the complexity of (photo)catalytic processes, and the numerous challenges related to rationalizing and optimizing the properties of catalysts, similar strategies would be of interest for other catalytic reactions which can involve oxygen exchange/transfer steps.

## Conclusion

In this manuscript, we have developed new and efficient labeling strategies for the  $^{17}\text{O}$  and  $^{18}\text{O}$ -labeling of two fatty acids which are of major interest in (bio)molecular chemistry and (nano)materials science: stearic acid and oleic acid.

Thanks to these enrichment schemes, new levels of structural insight could be reached for two systems which have been studied and used in a many research fields:<sup>44-45, 52, 54, 57, 83</sup> crystalline Zn oleate, and OA functionalized ZnO nanoparticles. The high level of  $^{17}\text{O}$ -labeling enabled high-resolution NMR analyses to be performed in reasonable experimental time, from which fine structural information could be obtained for the first time. In the former case, different bidentate bridging modes of oleate ligands to  $\text{Zn}^{2+}$  could be resolved, which were shown to differ in very small changes in the  $\text{Zn}\cdots\text{O}$  distances, estimated to only  $\sim 0.01$  Å. Such level of insight could not have been reached by more standard  $^{13}\text{C}$  solid state NMR analyses, which points to the added value of performing  $^{17}\text{O}$  NMR studies for helping understanding the structure of fatty-acid phases for which no crystal structure is yet available. In the latter case, direct insight into the mode of binding and reactivity of oleic acid molecules at the surface of ZnO was reached, by looking at the carboxylic oxygen atoms. The predominance of the oleate form at the nanoparticle surface was thereby demonstrated, and structural changes occurring after irradiation were evidenced, including the  $^{17}\text{O}$ -isotopic enrichment of the nanoparticle surface, which occurs in addition to the photodegradation processes of grafted  $^{17}\text{O}$ -labeled oleic acid molecules. This type of information on the reactivity of organic-mineral interfaces had not been provided so far, and could only have been accessed using  $^{17}\text{O}$  NMR. Given the number of studies aiming at understanding and optimizing photocatalytic processes taking place at the surface of ZnO nanoparticles, depending on their size and shape, being able to achieve such atomic-level insight will clearly be beneficial, by allowing to go one step further in comparison to more conventional spectroscopic analyses.<sup>9, 101, 104</sup>

The fine structural investigations described here were made possible by the high level of enrichment oxygen-isotope enrichment of the fatty acids, and the possibility to produce these enriched molecules on a large scale. Mechanochemistry was found to be very well suited for this purpose, allowing up to gram quantities of these labeled molecules to be obtained in high yield and at reasonable cost in just a few hours ( $\sim 1/2$  day of manipulation). Considering that very few protocols had been proposed so far for the oxygen-isotopic labeling of fatty acids, none of which was as efficient for  $^{17}\text{O}$  NMR purposes, this work clearly opens new perspectives for advanced structural studies of other complex molecular and materials systems involving fatty acids, such as other metal soaps, grafted nanoparticles (including with other photocatalysts like  $\text{TiO}_2$ ), or even more complex (nano)formulations, such as those developed for oil-paints, sunscreens, or nanolubricants. Moreover, the greater availability of the  $^{17}\text{O}$  or  $^{18}\text{O}$  enriched fatty acids is expected to also favor the development and use of other structural characterization techniques which are sensitive to the stable isotopes of oxygen, such as vibrational spectroscopies (IR and Raman), mass spectrometry (including high-resolution FT-ICR - Fourier Transform Ion Cyclotron Resonance),<sup>105</sup> as well as  $^{17}\text{O}$  QCT (quadrupole central transition) and  $^{17}\text{O}$  DNP-enhanced NMR spectroscopies.<sup>26</sup>

## ASSOCIATED CONTENT

**Supporting Information.** Materials and methods; experimental protocols and full characterizations of the  $^{17}\text{O}$  and  $^{18}\text{O}$ -labeled fatty acids; synthesis and structural characterizations of Zn-oleate (including GIPAW-DFT calculations of NMR parameters of Zn-alkanoate phases); synthesis and complementary characterization of grafted ZnO nanorods (including variable temperature  $^1\text{H}$  and  $^{17}\text{O}$  MAS NMR analyses). This material is available free of charge via the Internet at <http://pubs.acs.org>.

## AUTHOR INFORMATION

### Corresponding Authors

\* To whom correspondence should be addressed: [danielle.laurencin@umontpellier.fr](mailto:danielle.laurencin@umontpellier.fr) and [thomas-xavier.metro@umontpellier.fr](mailto:thomas-xavier.metro@umontpellier.fr).

## ACKNOWLEDGMENTS

This project has received funding from the European Research Council (ERC) under the European Union's Horizon 2020 research and innovation program (grant agreement No 772204; 2017 ERC-COG, MISOTOP project). A portion of this work was performed at the National High Magnetic Field Laboratory, which is supported by the National Science Foundation Cooperative Agreement No. DMR-1644779, the State of Florida and the United States Department of Energy. NMR spectroscopic calculations were performed using HPC resources from GENCI-IDRIS (Grant 097535). Development of the 36 T Series-Connected Hybrid magnet and NMR instrumentation was supported by National Science Foundation (DMR-1039938 and DMR-0603042) and National Institute of Health P41 GM122698. Dr Sylvie Bégu (ICGM) is acknowledged for her assistance in the use of the ATLAS SunTest/CPS+ apparatus, and Drs Ieva Goldberga and Philippe Gaveau for their assistance in the variable temperature NMR experiments. The anonymous referees are also acknowledged for valuable feedback on this work.

## REFERENCES and FOOTNOTES

- De Carvalho, C. C.; Caramujo, J. M., The Various Roles of Fatty Acids. *Molecules* **2018**, *23*, 2583.
- Spector, A. A.; Kim, H.-Y., Discovery of essential fatty acids. *J. Lipid Res.* **2015**, *56*, 11-21.
- Lynch, M. L., Acid-soaps. *Curr. Opin. Colloid Interf. Sci.* **1997**, *2*, 495-500.
- de Mul, M. N. G.; Davis, H. T.; Evans, D. F.; Bhave, A. V.; Wagner, J. R., Solution Phase Behavior and Solid Phase Structure of Long-Chain Sodium Soap Mixtures. *Langmuir* **2000**, *16* (22), 8276-8284.
- Mehnert, W.; Mäder, K., Solid lipid nanoparticles: Production, characterization and applications. *Adv. Drug Deliv. Rev.* **2012**, *64*, 83-101.
- Izgu, E. C.; Björkbohm, A.; Kamat, N. P.; Lelyveld, V. S.; Zhang, W.; Jia, T. Z.; Szostak, J. W., N-Carboxyanhydride-Mediated Fatty Acylation of Amino Acids and Peptides for Functionalization of Protocell Membranes. *J. Am. Chem. Soc.* **2016**, *138*, 16669-16676.
- Ulman, A., Formation and Structure of Self-Assembled Monolayers. *Chem. Rev.* **1996**, *96*, 1533-1554.
- Zherebetsky, D.; Scheele, M.; Zhang, Y.; Bronstein, N.; Thompson, C.; Britt, D.; Salmeron, M.; Alivisatos, P.; Wang, L.-W., Hydroxylation of the surface of PbS nanocrystals passivated with oleic acid. *Science* **2014**, *344*, 1380.
- Kwak, G.; Seol, M.; Tak, Y.; Yong, K., Superhydrophobic ZnO Nanowire Surface: Chemical Modification and Effects of UV Irradiation. *J. Phys. Chem. C*, **2009**, *113*, 12085-12089.
- Oliva-Puigdomènech, A.; De Roo, J.; Kuhs, J.; Detavernier, C.; Martins, J. C.; Hens, Z., Ligand Binding to Copper Nanocrystals: Amines and Carboxylic Acids and the Role of Surface Oxides. *Chem. Mater.* **2019**, *31*, 2058-2067.
- Zhang, J.; Zhang, H.; Cao, W.; Pang, Z.; Li, J.; Shu, Y.; Zhu, C.; Kong, X.; Wang, L.; Peng, X., Identification of Facet-Dependent Coordination Structures of Carboxylate Ligands on CdSe Nanocrystals. *J. Am. Chem. Soc.* **2019**, *141*, 15675-15683.
- Pang, Z.; Zhang, J.; Cao, W.; Kong, X.; Peng, X., Partitioning surface ligands on nanocrystals for maximal solubility. *Nature Comm.* **2019**, *10*, 2454.
- Pawsey, S.; Yach, K.; Halla, J.; Reven, L., Self-Assembled Monolayers of Alkanoic Acids: A Solid-State NMR Study. *Langmuir* **2000**, *16*, 3294-3303.
- Rowat, A. C.; Kitson, N.; Thewalt, J. L., Interactions of oleic acid and model stratum corneum membranes as seen by  $^2\text{H}$  NMR. *Int. J. Pharm.* **2006**, *307*, 225-231.
- Catalano, J.; Murphy, A.; Yao, Y.; Zumbulyadis, N.; Centeno, S. A.; Dybowski, C., Molecular dynamics of palmitic acid and lead palmitate in cross-linked linseed oil films: Implications from deuterium magnetic resonance for lead soap formation in traditional oil paintings. *Solid State Nucl. Magn. Reson.* **2018**, *89*, 21-26.
- Catalano, J.; Di Tullio, V.; Wagner, M.; Zumbulyadis, N.; Centeno, S. A.; Dybowski, C., Review of the use of NMR spectroscopy to investigate structure, reactivity, and dynamics of lead soap formation in paintings. *Magn. Reson. Chem.* **2020**, *58*, 798-811.
- Menzel, R.; Ngosong, C.; Ruess, L., Isotopologue profiling enables insights into dietary routing and metabolism of trophic biomarker fatty acids. *Chemoecology* **2017**, *27*, 101-114.
- Gotoh, N.; Nagai, T.; Yoshinaga, K.; Mizobe, H.; Watanabe, H., Comparison of catabolic rates of fatty acids using stable isotope and isotope-ratio mass spectrometry. *Lipid Technol.* **2013**, *25*, 110-112.
- Cun-nane, S. C.; Williams, S. C. R.; Bell, J. D.; Brookes, S.; Craig, K.; Iles, R. A.; Crawford, M. A., Utilization of Uniformly Labeled  $^{13}\text{C}$ -Polyunsaturated Fatty Acids in the Synthesis of Long-Chain Fatty Acids and Cholesterol Accumulating in the Neonatal Rat Brain. *J. Neurochem.* **1994**, *62*, 2429-2436.
- Crane, S. N.; Bateman, K.; Gagne, S.; Levesque, J.-F., Preparation of deuterium-labeled monounsaturated and saturated fatty acids for use as stable isotope metabolic tracers. *J. Label. Compd. Radiopharm.* **2006**, *49*, 1273-1285.
- Sparrow, J. T.; Patel, K. M.; Morrisett, J. D., Synthesis of carbon-13-labeled tetradecanoic acids. *J. Lipid Res.* **1983**, *24*, 938-941.
- El'man, A. R.; Batov, A. E. Process for preparation of carbon-13-labeled saturated aliphatic carboxylic acids by hydrocarboxylation of  $\alpha$ -olefins with labeled carbon monoxide and water and processes for preparing their derivatives. Patent # RU2311402C1, **2007**.
- Le, P. M.; Fraser, C.; Gardner, G.; Liang, W.-W.; Kralovec, J. A.; Cunneane, S. C.; Windust, A. J., Biosynthetic production of universally  $^{13}\text{C}$ -labelled polyunsaturated fatty acids as reference materials for natural health product research. *Anal. Bioanal. Chem.* **2007**, *389*, 241-249.
- Tortajada, A.; Duan, Y.; Sahoo, B.; Cong, F.; Toupalas, G.; Sallustrau, A.; Loreau, O.; Audisio, D.; Martin, R., Catalytic Decarboxylation/Carboxylation Platform for Accessing Isotopically Labeled Carboxylic Acids. *ACS Catal.* **2019**, *9*, 5897-5901.
- Vereshchagin, A. L.; Gorshkov, A. G.; Glyzina, O. Y.; Belikova, A. S.; Basharina, T. N.; Lyubochko, S. A.; Volokitina, N. A. Method for obtaining  $^{13}\text{C}$  isotope labeled polyunsaturated fatty acids. Patent #RU2361922C1, **2009**.

26. Wu, G.,  $^{17}\text{O}$  NMR studies of organic and biological molecules in aqueous solution and in the solid state. *Prog. Nucl. Magn. Reson. Spectrosc.* **2019**, *114-115*, 135-191.
27. Wu, G., Solid-State  $^{17}\text{O}$  NMR studies of organic and biological molecules: Recent advances and future directions. *Solid State Nucl. Magn. Reson.* **2016**, *73*, 1-14.
28. Keeler, E. G.; Michaelis, V. K.; Wilson, C. B.; Hung, I.; Wang, X.; Gan, Z.; Griffin, R. G., High-Resolution  $^{17}\text{O}$  NMR Spectroscopy of Structural Water. *J. Phys. Chem. B* **2019**, *123*, 3061-3067.
29. Perras, F. A.; Wang, Z.; Naik, P.; Slowing, I. I.; Pruski, M., Natural Abundance  $^{17}\text{O}$  DNP NMR Provides Precise O-H Distances and Insights into the Brønsted Acidity of Heterogeneous Catalysts. *Angew. Chem. Int. Ed.* **2017**, *56*, 9165-9169.
30. Bignami, G. P. M.; Davis, Z. H.; Dawson, D. M.; Morris, S. A.; Russell, S. E.; McKay, D.; Parke, R. E.; Iuga, D.; Morris, R. E.; Ashbrook, S. E., Cost-effective  $^{17}\text{O}$  enrichment and NMR spectroscopy of mixed-metal terephthalate metal-organic frameworks. *Chem. Sci.* **2018**, *9*, 850-859.
31. Martins, V.; Xu, J.; Wang, X.; Chen, K.; Hung, I.; Gan, Z.; Gervais, C.; Bonhomme, C.; Jiang, S.; Zheng, A.; Lucier, B. E. G.; Huang, Y., Higher Magnetic Fields, Finer MOF Structural Information:  $^{17}\text{O}$  Solid-State NMR at 35.2 T. *J. Am. Chem. Soc.* **2020**, *142*, 14877-14889.
32. Ashbrook, S. E.; Smith, M. E., Solid state  $^{17}\text{O}$  NMR—an introduction to the background principles and applications to inorganic materials. *Chem. Soc. Rev.* **2006**, *35*, 718-735.
33. Tsuchihashi, Y. Oxygen isotope-labeled carboxylic acid salt compound, reagent for oxygen isotope labeling, method for producing oxygen isotope-labeled carboxylic acid salt compound, and method for producing oxygen isotope-labeled alcohol. Patent # JP2020037545A, **2020**.
34. Jiang, X.; Zhang, J.; Ma, S., Iron Catalysis for Room-Temperature Aerobic Oxidation of Alcohols to Carboxylic Acids. *J. Am. Chem. Soc.* **2016**, *138*, 8344-8347.
35. Gallego, F. S.; Hermansson, M.; Liebisch, G.; Hodson, L.; Ejsing, S. C., Total Fatty Acid Analysis of Human Blood Samples in One Minute by High-Resolution Mass Spectrometry. *Biomolecules* **2019**, *9*, 7.
36. Friščić, T.; Mottillo, C.; Titi, H. M., Mechanochemistry for Synthesis. *Angew. Chem. Int. Ed.* **2019**, *59*, 1018-1029.
37. Howard, Joseph L.; Cao, Q.; Browne, D. L., Mechanochemistry as an emerging tool for molecular synthesis: what can it offer? *Chem. Sci.* **2018**, *9*, 3080-3094.
38. Boldyreva, E., Mechanochemistry of inorganic and organic systems: what is similar, what is different? *Chem. Soc. Rev.* **2013**, *42*, 7719-7738.
39. James, S. L.; Adams, C. J.; Bolm, C.; Braga, D.; Collier, P.; Friščić, T.; Grepioni, F.; Harris, K. D. M.; Hyett, G.; Jones, W.; Krebs, A.; Mack, J.; Maini, L.; Orpen, A. G.; Parkin, I. P.; Shearouse, W. C.; Steed, J. W.; Waddell, D. C., Mechanochemistry: opportunities for new and cleaner synthesis. *Chem. Soc. Rev.* **2012**, *41*, 413-447.
40. Friščić, T.; Childs, S. L.; Rizvi, S. A. A.; Jones, W., The role of solvent in mechanochemical and sonochemical cocrystal formation: a solubility-based approach for predicting cocrystallisation outcome. *CrystEngComm* **2009**, *11*, 418-426.
41. Hasa, D.; Miniussi, E.; Jones, W., Mechanochemical Synthesis of Multicomponent Crystals: One Liquid for One Polymorph? A Myth to Dispel. *Crystal Growth Des.* **2016**, *16*, 4582-4588.
42. Métro, T.-X.; Gervais, C.; Martinez, A.; Bonhomme, C.; Laurencin, D., Unleashing the Potential of  $^{17}\text{O}$  NMR Spectroscopy Using Mechanochemistry. *Angew. Chem. Int. Ed.* **2017**, *129*, 6907-6911.
43. Chen, C.-H.; Gaillard, E.; Mentink-Vigier, F.; Chen, K.; Gan, Z.; Gaveau, P.; Rebière, B.; Berthelot, R.; Florian, P.; Bonhomme, C.; Smith, M. E.; Métro, T.-X.; Alonso, B.; Laurencin, D., Direct  $^{17}\text{O}$  Isotopic Labeling of Oxides Using Mechanochemistry. *Inorg. Chem.* **2020**, *59*, 13050-13066.
44. Hermans, J. J.; Baij, L.; Koenis, M.; Keune, K.; Iedema, P. D.; Woutersen, S., 2D-IR spectroscopy for oil paint conservation: Elucidating the water-sensitive structure of zinc carboxylate clusters in ionomers. *Science Adv.* **2019**, *5*, eaaw3592.
45. Yin, H.; Casey, P. S.; McCall, M. J.; Fenech, M., Effects of Surface Chemistry on Cytotoxicity, Genotoxicity, and the Generation of Reactive Oxygen Species Induced by ZnO Nanoparticles. *Langmuir* **2010**, *26*, 15399-15408.
46. Ha, S.-T.; Su, R.; Xing, J.; Zhang, Q.; Xiong, Q., Metal halide perovskite nanomaterials: synthesis and applications. *Chem. Sci.* **2017**, *8*, 2522-2536.
47. Cai, J.; Miao, Y. Q.; Yu, B. Z.; Ma, P.; Li, L.; Fan, H. M., Large-Scale, Facile Transfer of Oleic Acid-Stabilized Iron Oxide Nanoparticles to the Aqueous Phase for Biological Applications. *Langmuir* **2017**, *33*, 1662-1669.
48. Shah, R. M.; Rajasekaran, D.; Ludford-Menting, M.; Eldridge, D. S.; Palombo, E. A.; Harding, I. H., Transport of stearic acid-based solid lipid nanoparticles (SLNs) into human epithelial cells. *Coll. Surf. B: Biointerf.* **2016**, *140*, 204-212.
49. Otero, V.; Sanches, D.; Montagner, C.; Vilarigues, M.; Carlyle, L.; Lopes, J. A.; Melo, M. J., Characterisation of metal carboxylates by Raman and infrared spectroscopy in works of art. *J. Raman Spectrosc.* **2014**, *45*, 1197-1206.
50. Robinet, L.; Corbeil, M.-C., The Characterization of Metal Soaps. *Studies Conserv.* **2003**, *48*, 23-40.
51. Maines, C. A.; Rogala, D.; Lake, S.; Mecklenburg, M., Deterioration in Abstract Expressionist Paintings: Analysis of Zinc Oxide Paint Layers in Works from the Collection of the Hirshhorn Museum and Sculpture Garden, Smithsonian Institution. *MRS Proceedings* **2011**, *1319*, mrsf10-1319-ww04-01.
52. Glassy, B. A.; Cossairt, B. M., Ternary synthesis of colloidal  $\text{Zn}_3\text{P}_2$  quantum dots. *Chem. Commun.* **2015**, *51*, 5283-5286.
53. Zhang, L.; Yin, L.; Wang, C.; Lun, N.; Qi, Y.; Xiang, D., Origin of Visible Photoluminescence of ZnO Quantum Dots: Defect-Dependent and Size-Dependent. *J. Phys. Chem. C* **2010**, *114*, 9651-9658.
54. Fang, X.; Jiang, L.; Gong, Y.; Li, J.; Liu, L.; Cao, Y., The presence of oleate stabilized ZnO nanoparticles (NPs) and reduced the toxicity of aged NPs to Caco-2 and HepG2 cells. *Chemico-Biol. Interact.* **2017**, *278*, 40-47.
55. Smijs, T. G.; Pavel, S., Titanium dioxide and zinc oxide nanoparticles in sunscreens: focus on their safety and effectiveness. *Nanotechnol. Sci. Appl.* **2011**, *4*, 95-112.
56. Artesani, A.; Gherardi, F.; Nevin, A.; Valentini, G.; Comelli, D., A Photoluminescence Study of the Changes Induced in the Zinc White Pigment by Formation of Zinc Complexes. *Materials* **2017**, *10*, 340.
57. Baij, L.; Hermans, J. J.; Keune, K.; Iedema, P., Time-Dependent ATR-FTIR Spectroscopic Studies on Fatty Acid Diffusion and the Formation of Metal Soaps in Oil Paint Model Systems. *Angew. Chem. Int. Ed.* **2018**, *57*, 7351-7354.
58. Fanelli, F.; Mastrangelo, A. M.; Fracassi, F., Aerosol-Assisted Atmospheric Cold Plasma Deposition and Characterization of Superhydrophobic Organic-Inorganic Nanocomposite Thin Films. *Langmuir* **2014**, *30*, 857-865.
59. Métro, T.-X.; Martinez, J.; Lamaty, F., 1,1'-Carbonyldiimidazole and Mechanochemistry: A Shining Green Combination. *ACS Sustainable Chem. Eng.* **2017**, *5*, 9599-9602.
60. Kaneko, F.; Simofuku, T.; Miyamoto, H.; Kobayashi, M.; Suzuki, M., Vibrational spectroscopic study on the occurrence of stearic acid B and E forms: heterogeneous nucleation of the B form on the surface of E crystals and the topotactic phase transition from E to B. *J. Phys. Chem.* **1992**, *96*, 10554-10559.
61. Pudney, P. D. A.; Mutch, K. J.; Zhu, S., Characterising the phase behaviour of stearic acid and its triethanolamine soap and acid-soap by infrared spectroscopy. *Phys. Chem. Chem. Phys.* **2009**, *11*, 5010-5018.



62. Zerbi, G.; Conti, G.; Minoni, G.; Pison, S.; Bigotto, A., Premelting phenomena in fatty acids: an infrared and Raman study. *J. Phys. Chem.* **1987**, *91*, 2386-2393.
63. Different synthetic batches of each  $^{17}\text{O}$  or  $^{18}\text{O}$  enriched molecule were analyzed by IR, showing that the wavenumbers and trends reported here are robust.
64. Wong, A.; Poli, F., Chapter Three - Solid-State  $^{17}\text{O}$  NMR Studies of Biomolecules. In *Ann. Rep. NMR Spectrosc.*, Webb, G. A., Ed. Academic Press: 2014; Vol. 83, pp 145-220.
65. Moreno-Calvo, E.; Gbabode, G.; Cordobilla, R.; Calvet, T.; Cuevas-Diarte, M. Á.; Negrier, P.; Mondieig, D., Competing Intermolecular Interactions in the High-Temperature Solid Phases of Even Saturated Carboxylic Acids ( $\text{C}_{10}\text{H}_{19}\text{O}_2\text{H}$  to  $\text{C}_{20}\text{H}_{39}\text{O}_2\text{H}$ ). *Chem. -Eur. J.* **2009**, *15*, 13141-13149.
66. Kaneko, F.; Yamazaki, K.; Kitagawa, K.; Kikyo, T.; Kobayashi, M.; Kitagawa, Y.; Matsuura, Y.; Sato, K.; Suzuki, M., Structure and Crystallization Behavior of the  $\beta$  Phase of Oleic Acid. *J. Phys. Chem. B*, **1997**, *101*, 1803-1809.
67. Moreno, E.; Cordobilla, R.; Calvet, T.; Cuevas-Diarte, M. A.; Gbabode, G.; Negrier, P.; Mondieig, D.; Oonk, H. A. J., Polymorphism of even saturated carboxylic acids from n-decanoic to n-eicosanoic acid. *New J. Chem.* **2007**, *31*, 947-957.
68. Wang, L.; Uribe-Romo, F. J.; Mueller, L. J.; Harper, J. K., Predicting anisotropic thermal displacements for hydrogens from solid-state NMR: a study on hydrogen bonding in polymorphs of palmitic acid. *Phys. Chem. Chem. Phys.* **2018**, *20*, 8475-8487.
69. Gbabode, G.; Negrier, P.; Mondieig, D.; Moreno, E.; Calvet, T.; Cuevas-Diarte, M. Á., Fatty acids polymorphism and solid-state miscibility: Pentadecanoic acid-hexadecanoic acid binary system. *J. Alloys Compds*, **2009**, *469*, 539-551.
70. Kong, X.; Shan, M.; Tersikh, V.; Hung, I.; Gan, Z.; Wu, G., Solid-State  $^{17}\text{O}$  NMR of Pharmaceutical Compounds: Salicylic Acid and Aspirin. *J. Phys. Chem. B*, **2013**, *117*, 9643-9654.
71. Wu, G.; Hung, I.; Gan, Z.; Tersikh, V.; Kong, X., Solid-State  $^{17}\text{O}$  NMR Study of Carboxylic Acid Dimers: Simultaneously Accessing Spectral Properties of Low- and High-Energy Tautomers. *J. Phys. Chem. A*, **2019**, *123*, 8243-8253.
72. Zeleňák, V.; Vargová, Z.; Györyová, K., Correlation of infrared spectra of zinc(II) carboxylates with their structures. *Spectrochim. Acta A: Mol. Biomol. Spectrosc.* **2007**, *66*, 262-272.
73. Ishioka, T.; Shibata, Y.; Takahashi, M.; Kanesaka, I., Vibrational spectra and structures of zinc carboxylates II. Anhydrous zinc acetate and zinc stearate. *Spectrochim. Acta A: Mol. Biomol. Spectrosc.* **1998**, *54*, 1811-1818.
74. Mesbah, A. I) Cristallochimie des Carboxylates Métalliques Inhibiteurs de la Corrosion de Métaux et II) Structure et Magnétisme de Dicarboxylates (téréphtalate et thiophène) de Métaux de Transition. PhD thesis, **2008**.
75. A splitting of the carboxylate and  $\alpha\text{-CH}_2$  resonances was also observed on the  $^{13}\text{C}$  CPMAS NMR spectra of a Zn-oleate phase synthesized by the same procedure, but using non-enriched oleic acid.
76. Pickard, C. J.; Mauri, F., All-electron magnetic response with pseudopotentials: NMR chemical shifts. *Phys. Rev. B* **2001**, *63*, 245101.
77. Charpentier, T., The PAW/GIPAW approach for computing NMR parameters: A new dimension added to NMR study of solids. *Sol. St. Nucl. Magn. Reson.* **2011**, *40*, 1-20.
78. Harris, R. A.; van der Walt, H.; Shumbula, P. M., Engineered Inorganic/Organic-Core/Shell Magnetic  $\text{Fe}_x\text{O}_y$  Nanoparticles with Oleic Acid and/or Oleylamine As Capping Agents. *Curr. Pharm. Des.* **2015**, *21*, 5369-5388.
79. Sun, S.; Zeng, H.; Robinson, D. B.; Raoux, S.; Rice, P. M.; Wang, S. X.; Li, G., Monodisperse  $\text{MFe}_2\text{O}_4$  ( $\text{M} = \text{Fe}, \text{Co}, \text{Mn}$ ) Nanoparticles. *J. Am. Chem. Soc.* **2004**, *126*, 273-279.
80. Sun, S.; Murray, C. B.; Weller, D.; Folks, L.; Moser, A., Monodisperse FePt Nanoparticles and Ferromagnetic FePt Nanocrystal Superlattices. *Science* **2000**, *287*, 1989.
81. Sun, S.; Zeng, H., Size-Controlled Synthesis of Magnetite Nanoparticles. *J. Am. Chem. Soc.* **2002**, *124*, 8204-8205.
82. Wu, N.; Fu, L.; Su, M.; Aslam, M.; Wong, K. C.; Dravid, V. P., Interaction of Fatty Acid Monolayers with Cobalt Nanoparticles. *Nano Lett.* **2004**, *4*, 383-386.
83. McLaren, A.; Valdes-Solis, T.; Li, G.; Tsang, S. C., Shape and Size Effects of ZnO Nanocrystals on Photocatalytic Activity. *J. Am. Chem. Soc.* **2009**, *131*, 12540-12541.
84. Wang, H.; Lian, Y., A mechanistic study of oleic acid-mediated solvothermal shape controllable preparation of zinc oxide nanostructures. *J. Alloys Compds*, **2014**, *594*, 141-147.
85. Chen, L.; Holmes, J. D.; Ramírez-García, S.; Morris, M. A., Facile Synthesis of Monodisperse ZnO Nanocrystals by Direct Liquid Phase Precipitation. *J. Nanomat.* **2011**, *2011*, 853832.
86. Chen, L.; Xu, J.; Holmes, J. D.; Morris, M. A., A Facile Route to ZnO Nanoparticle Superlattices: Synthesis, Functionalization, and Self-Assembly. *J. Phys. Chem. C* **2010**, *114*, 2003-2011.
87. Pacholski, C.; Kornowski, A.; Weller, H., Self-Assembly of ZnO: From Nanodots to Nanorods. *Angew. Chem. Int. Ed.* **2002**, *41*, 1188-1191.
88. Sun, B.; Sirringhaus, H., Solution-Processed Zinc Oxide Field-Effect Transistors Based on Self-Assembly of Colloidal Nanorods. *Nano Lett.* **2005**, *5*, 2408-2413.
89. Lee, D.; Wolska-Pietkiewicz, M.; Badoni, S.; Grala, A.; Lewiński, J.; De Paëpe, G., Disclosing Interfaces of ZnO Nanocrystals Using Dynamic Nuclear Polarization: Sol-Gel versus Organometallic Approach. *Angew. Chem. Int. Ed.* **2019**, *58*, 17163-17168.
90. Noei, H.; Wöll, C.; Muhler, M.; Wang, Y., Activation of Carbon Dioxide on ZnO Nanoparticles Studied by Vibrational Spectroscopy. *J. Phys. Chem. C* **2011**, *115*, 908-914.
91. Gankanda, A.; Cwiertny, D. M.; Grassian, V. H., Role of Atmospheric  $\text{CO}_2$  and  $\text{H}_2\text{O}$  Adsorption on ZnO and CuO Nanoparticle Aging: Formation of New Surface Phases and the Impact on Nanoparticle Dissolution. *J. Phys. Chem. C*, **2016**, *120*, 19195-19203.
92. Andelman, T.; Gong, Y.; Polking, M.; Yin, M.; Kuskovsky, I.; Neumark, G.; O'Brien, S., Morphological Control and Photoluminescence of Zinc Oxide Nanocrystals. *J. Phys. Chem. B*, **2005**, *109*, 14314-14318.
93. Hong, R.; Pan, T.; Qian, J.; Li, H., Synthesis and surface modification of ZnO nanoparticles. *Chem. Eng. J.* **2006**, *119*, 71-81.
94. It is worth noting that the  $\text{CH}_2$  resonance in  $\alpha$  of the carboxylic group was also found to be broad, and clearly shifted to high frequencies compared to a concentrated solution of oleic acid in  $\text{DMSO-}d_6$  (37.5 vs 33.8 ppm), as expected upon grafting of fatty acids at the surface of oxide nanoparticles (cf ref. 13). This implies that this  $\text{CH}_2$  moiety is not as mobile as the others.
95. Although the  $^{13}\text{C}$  chemical shift of the grafted acetate groups is very similar to the one of oleic acid-functionalized NPs (180.5 vs 181.1 ppm), the amount of residual surface acetates after functionalization by oleic acid is small, as shown in supporting information (Figure D1S9).
96. For a very concentrated solution of oleic acid in  $\text{DMSO-}d_6$  (i.e. for a  $\sim 94/6$  v/v ratio between oleic acid and  $\text{DMSO}$ ), the  $^{13}\text{C}$  solution NMR spectrum at room temperature was recorded. The  $^{13}\text{C}$  carboxylic resonance was found at 178.03 ppm, and the  $\alpha\text{-CH}_2$  group at 33.8 ppm.
97. Champouret, Y.; Coppel, Y.; Kahn, M. L., Evidence for Core Oxygen Dynamics and Exchange in Metal Oxide Nanocrystals from In Situ  $^{17}\text{O}$  MAS NMR. *J. Am. Chem. Soc.* **2016**, *138*, 16322-16328.
98. Spataro, G.; Champouret, Y.; Florian, P.; Coppel, Y.; Kahn, M. L., Multinuclear solid-state NMR study: a powerful tool for understanding the structure of ZnO hybrid nanoparticles. *Phys. Chem. Chem. Phys.* **2018**, *20*, 12413-12421.
99. Gerathanassis, I. P., Oxygen-17 NMR spectroscopy: Basic principles and applications (Part I). *Progr. Nucl. Magn. Reson. Spectrosc.* **2010**, *56*, 95-197.

100. Peng, Y.-K.; Tsang, S. C. E., Facet-dependent photocatalysis of nanosize semiconductive metal oxides and progress of their characterization. *Nano Today* **2018**, *18*, 15-34.
101. Kenanakis, G.; Giannakoudakis, Z.; Vernardou, D.; Savvakis, C.; Katsarakis, N., Photocatalytic degradation of stearic acid by ZnO thin films and nanostructures deposited by different chemical routes. *Catal. Today* **2010**, *151*, 34-38.
102. In b/, the slight increase in intensity observed between 5° and 10° on the powder patterns on the grafted NRs (black) and after 6h irradiation (blue) is due to the nature of the sample holder used for these analyses.
103. Ong, C. B.; Ng, L. Y.; Mohammad, A. W., A review of ZnO nanoparticles as solar photocatalysts: Synthesis, mechanisms and applications. *Renew. Sust. En. Rev.* **2018**, *81*, 536-551.
104. Yin, M.; Gu, Y.; Kuskovsky, I. L.; Andelman, T.; Zhu, Y.; Neumark, G. F.; O'Brien, S., Zinc Oxide Quantum Rods. *J. Am. Chem. Soc.* **2004**, *126*, 6206-6207.
105. Griffiths, W. J.; Wang, Y., Mass spectrometry: from proteomics to metabolomics and lipidomics. *Chem. Soc. Rev.* **2009**, *38*, 1882-1896.

